Part V

Appendices

Appendix A

Measurement of Acoustic Velocity Fluctuations using the Two Microphone Technique

A.1 Introduction

A number of velocity measurement techniques and instrumentation have been implemented for the past many years, to perform the standard task of flow field characterization and instantaneous velocity measurement. Quite a few of these techniques are very elaborate and require expensive hardware. Normally to obtain instantaneous measurement values, a large amount of post processing is required. Most of the standard velocity measurement tools are limited in their application to turbulent flows, and may not be accurate enough to measure small acoustic perturbations, that are essential for the experimental characterization of flame dynamics. Thus, for the purpose of measuring small perturbations in the velocity of the reactants just upstream of the flame, a velocity probe was designed based on the principles of an intensity probe.

Figure A.1: Velocity probe

A.2 Velocity Probe Description

The velocity probe, Figure A.1, consists of two microphones that are separated by a known distance. The simultaneously sampled signal from the two microphones is then processed through an electronic circuit to generate an instantaneous velocity signal.

A.2.1 Principle of Operation

The working of the entire device is based on Euler's equation:

$$-\bigtriangledown P = \rho \left[\frac{\partial U}{\partial t} + (U \cdot \bigtriangledown) U \right] \tag{A.1}$$

Restricting the analysis to the direction of the velocity probe (1-D analysis), equation A.1 becomes

$$-\frac{\partial P}{\partial x} = \rho \left[\frac{\partial U}{\partial t} + U \frac{\partial U}{\partial x} \right] \tag{A.2}$$

where P is the total pressure and U is the total velocity and ρ is the density. Let

$$P = \overline{p} + p' \tag{A.3}$$

$$U = \overline{u} + u' \tag{A.4}$$

where $\overline{p}$ and $\overline{u}$ are the mean pressure and velocity respectively, while p' and u' are the time varying components of pressure and velocity respectively. Substituting equations A.3 and A.4 in A.2, the following is obtained.

$$-\frac{\partial \overline{p}}{\partial x} - \frac{\partial p'}{\partial x} = \rho \left\{ \frac{\partial \overline{u}}{\partial t} + \frac{\partial u'}{\partial t} + (\overline{u} + u') \left[\frac{\partial \overline{u}}{\partial x} + \frac{\partial u'}{\partial x} \right] \right\} \tag{A.5}$$

Satisfying the momentum equation for mean flow and noting that the mean flow is steady and incompressible, equation A.5 reduces to

$$-\frac{\partial p'}{\partial x} = \rho \left\{ \frac{\partial u'}{\partial t} + \overline{u}\frac{\partial u'}{\partial x} + u'\frac{\partial u'}{\partial x} \right\} \tag{A.6}$$

Non-dimensionalize A.6 with

$$\widetilde{p'} = \frac{p'}{P_o} \ , \ \widetilde{u'} = \frac{u'}{c} \ , \ \widetilde{x} = \frac{x}{L} \ , \ \widetilde{\rho} = \frac{\rho}{\rho_{ref}} \ , \ \tau = \omega t$$

where P_o is the combustor pressure

c is the speed of sound

ω is the acoustic frequency

L is the acoustic wavelength

Thus,

$$-\frac{P_o}{L}\frac{\partial \widetilde{p'}}{\partial \widetilde{x}} = \rho_{ref}\,\widetilde{\rho} \left\{ \omega c \frac{\partial \widetilde{u'}}{\partial \tau} + \frac{c^2\,\widetilde{\overline{u}}}{L}\frac{\partial \widetilde{u'}}{\partial \widetilde{x}} + \frac{c^2\,\widetilde{u'}}{L}\frac{\partial \widetilde{u'}}{\partial \widetilde{x}} \right\} \tag{A.7}$$

Therefore,

$$-\frac{\partial \widetilde{p'}}{\partial \widetilde{x}} = \frac{\rho_{ref}\,\widetilde{\rho}\,c^2}{P_o} \left\{ \frac{\partial \widetilde{u'}}{\partial \tau} + \widetilde{\overline{u}}\frac{\partial \widetilde{u'}}{\partial \widetilde{x}} + \widetilde{u'}\frac{\partial \widetilde{u'}}{\partial \widetilde{x}} \right\} \tag{A.8}$$

For flows with Mach number below 0.1

$$\widetilde{\overline{u}}\frac{\partial \widetilde{u'}}{\partial \widetilde{x}} \equiv O\left(\epsilon^2\right) \ , \ \widetilde{u'}\frac{\partial \widetilde{u'}}{\partial \widetilde{x}} \equiv O\left(\epsilon^2\right)$$

and are neglected. Therefore, for low Mach number flows, equation A.6 reduces to

$$-\frac{\partial p'}{\partial x} = \rho \frac{\partial u'}{\partial t} \tag{A.9}$$

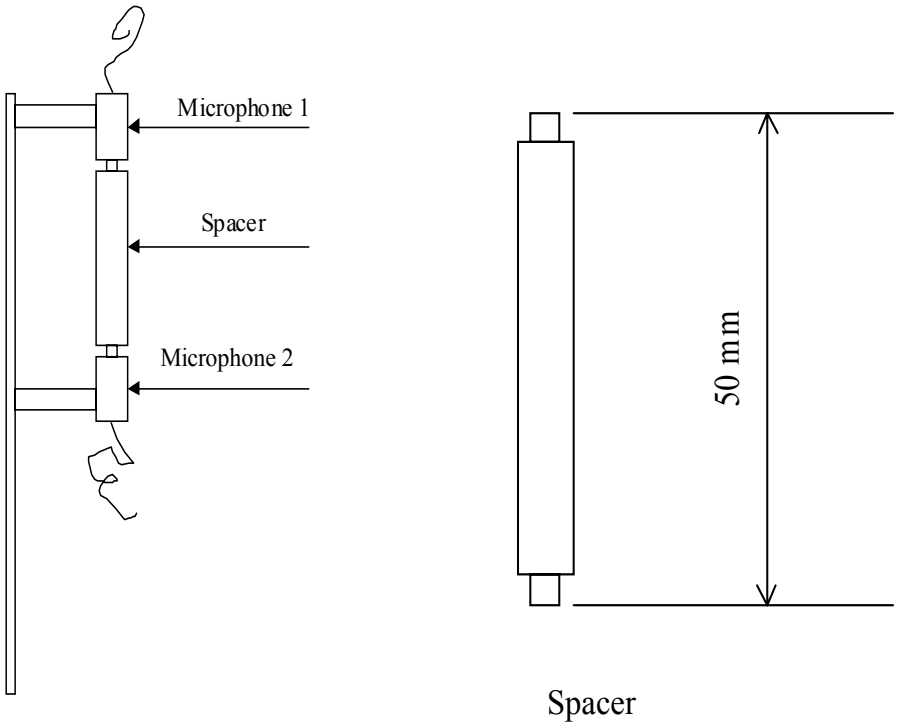

Figure A.2: Sketch of the velocity probe

Thus,

$$u'(t) = \frac{-1}{\rho} \int \frac{\partial p'}{\partial x} \, \partial t \tag{A.10}$$

The time trace of the instantaneous velocity fluctuations were generated using equation A.10, where the spatial derivative of pressure was approximated as

$$\frac{\partial p'}{\partial x} = \frac{P_2 - P_1}{\Delta x} \tag{A.11}$$

Here P_2 and P_1 are the simultaneous, instantaneous signals from the two microphones and Δx is the spatial distance between the two microphones.

A.2.2 Probe Sensor

A sketch of the probe sensor is shown in Figure A.2. Two microphones, Radio Shack catalogue number 33-3003 were used. These are tie clip condenser microphones that require a 1.5

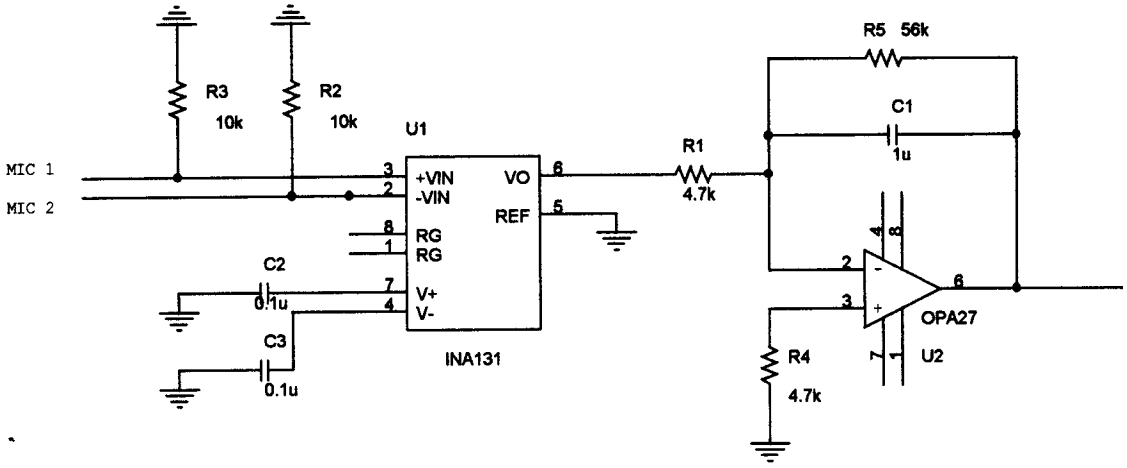

Figure A.3: Velocity probe circuit diagram

Volt external power source and are $\frac{1}{4}$" inch in diameter (see specifications in section A.4.3). The microphones were positioned so that they directly faced each other. A solid spacer as shown in Figure A.2, was placed between them. The spacer ensured that a fixed spatial distance was maintained between that two microphones and also prevented defraction of the sound around the microphones. The acoustic flow over the whole sensor was expected to be smoother with the spacers in place. Based on the analysis presented by Waser et al. [72], the length of the spacer was chosen to be 55 mm so that accurate data could be obtained in the frequency range of 20-1250 Hz.

A.2.3 Probe Circuit

To be able to generate a time trace of the fluctuating acoustic velocity as per equation A.10 and A.11, the signals from the two microphones were sent through a differencing amplifier, the output of which was fed into a low pass filter. Figure A.3 shows details of the electronic circuit, while Figure A.4 shows the details of the Burr-Brown precision gain instrumentation amplifier [89], that was used to generate a differencing signal. The technical specifications of the operational amplifier and the instrumentation amplifier are detailed in Section A.4.1 and Section A.4.2 respectively.

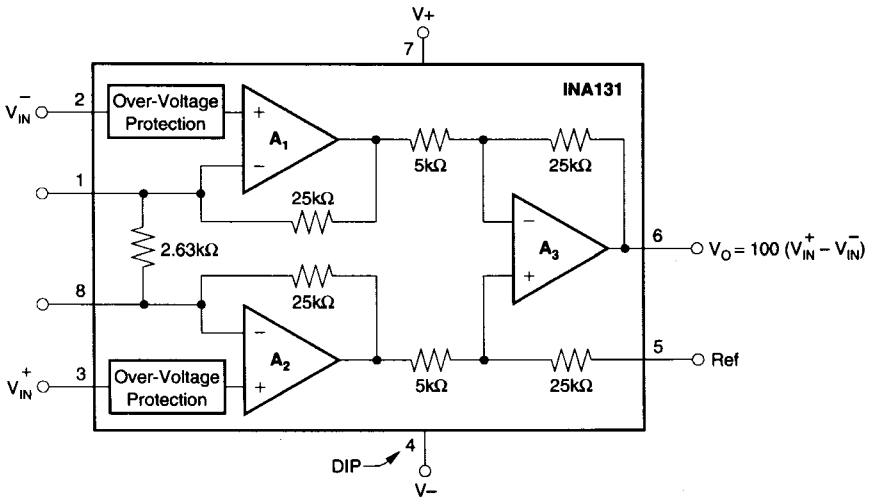

Figure A.4: Details of the Burr-Brown instrumentation amplifier INA 131

A.3 Calibration

A.3.1 Microphone Calibration

The microphones used in the velocity sensor were calibrated to ensure that their amplitude and phase matching characteristics were satisfactory. The FRF magnitude and phase of microphone '1' with respect to microphone '2' are shown in Figure A.5 and Figure A.6 respectively. Each of the Radio Shack microphones was held on a Bruel & Kjaer microphone calibrator registered at 94 dB at 1000 Hz. The voltage of 3.855 mV produced at 1000 Hz was recorded as the sensitivity of the microphone. Since 94 dB corresponds to 1.00237 Pa, the pressure calibration for the microphone is 260.018 Pa/volt.

A.3.2 Electronic Circuit Calibration

Let X volts be the actual difference in the voltage of the two microphones and A(ω) be the frequency dependent gain through the circuit. Then the output voltage (u_v) from the circuit,

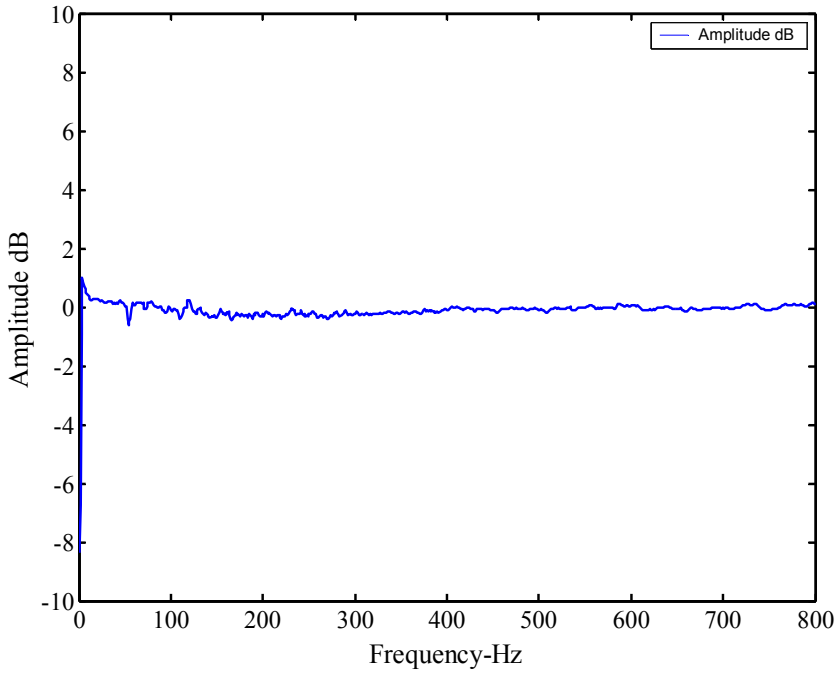

Figure A.5: FRF (magnitude) of microphone 1 and 2

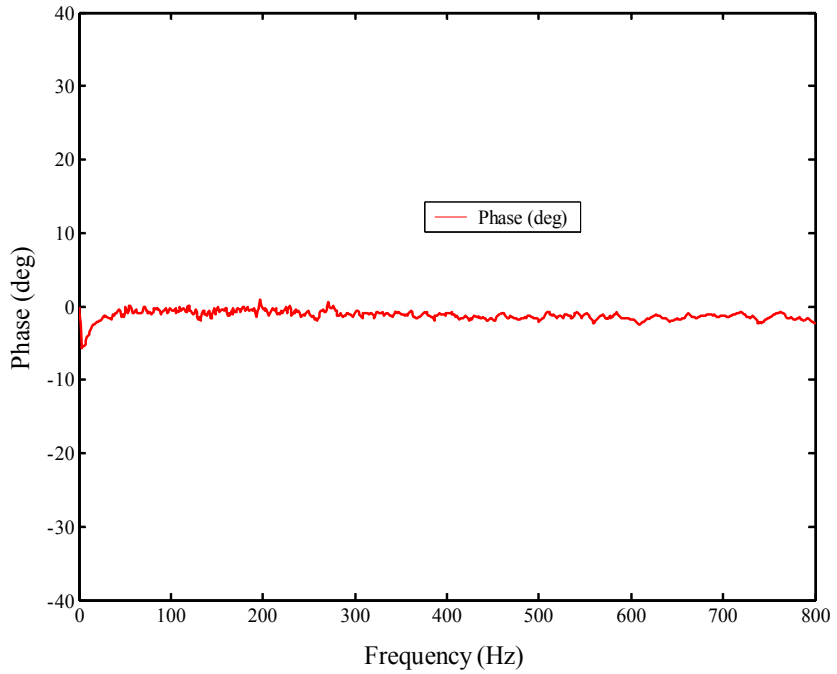

Figure A.6: FRF (phase) of microphone 1 and 2

measured in volts is given by

$$u_v = \frac{X[A(\omega)]}{j\omega} \tag{A.12}$$

Therefore,

$$X = \frac{j\omega}{A(\omega)} u_v \tag{A.13}$$

We know that the pressure calibration is 260.018 Pa/volt. Thus, the differential pressure is

$$\Delta P = 260.018\,(X) \tag{A.14}$$

Therefore using equations A.10 and A.11

$$u' = \frac{260.018}{\rho \Delta x} \int X dt \tag{A.15}$$

Performing a Laplace transform

$$u' = \frac{260.018}{\rho \Delta x} \frac{X}{j\omega} \tag{A.16}$$

Substituting for X from A.13

$$u' = \frac{260.018}{\rho \Delta x} \frac{u_v}{A\,(\omega)} \tag{A.17}$$

Equation A.17 gives velocity fluctuations in m/sec, while u_v is in $volts$.

The magnitude of the frequency response of the circuit to a two mV differential input is shown in Figure A.7. The two mV differential output was generated by grounding one of the inputs, and applying a two mV random noise signal to the other input. The random noise signal was generated using a Hewlett Packard dynamic signal analyzer. The corner frequency of the circuit is about 2 Hz. To obtain a frequency dependent gain A(ω), we compare the frequency response output of the circuit to that of a pure integrator. Since the lower frequency limit of the velocity probe is 20 Hz, which is greater than the circuit's corner frequency of 2 Hz, the slope, 20 dB drop in magnitude per decade of increase in frequency is achieved at 20 Hz and is maintained right through the bandwidth. Therefore the gain A(ω) can be taken as constant in the bandwidth of interest. The gain is evaluated by comparing the actual magnitude of the frequency response at 1000 radians (159.1549 Hz) with that of a pure integrator at the same frequency. A pure integrator should exhibit a magnitude of

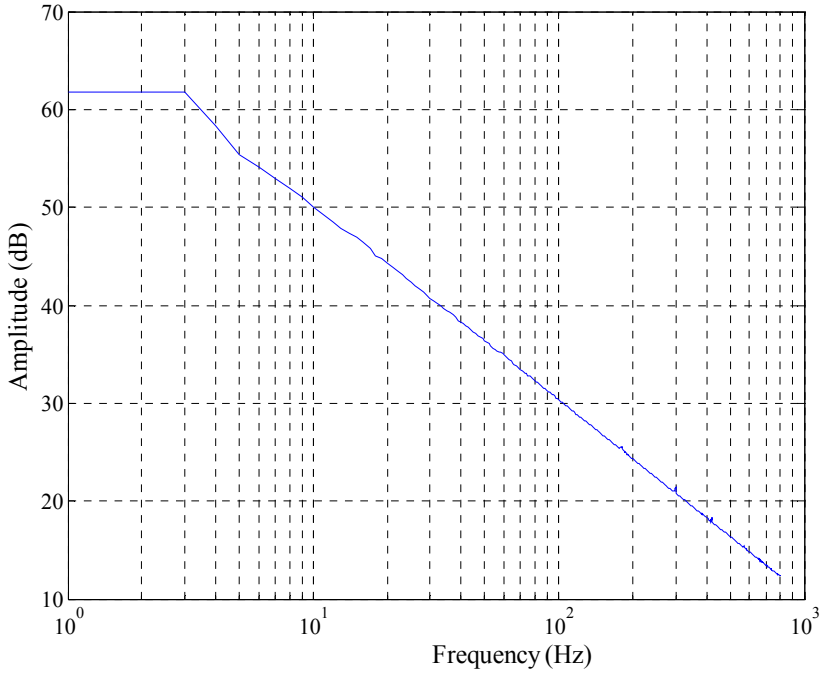

Figure A.7: The FRF magnitude of the velocity probe circuit to 2 mV random noise input

-60 dB at 1000 radians, while from Figure A.7 the magnitude of the circuit response at 1000 radians is found to be 26.3103 dB. Therefore, the gain A(ω) is given as

$$A(\omega) = \frac{10^{(\frac{26.3103}{20})}}{0.001} \tag{A.18}$$

Substituting equation A.18 into equation A.17

$$u' = \frac{0.012574}{\rho \Delta x} u_v \tag{A.19}$$

where u' is in m/sec, Δx is in meters, and ρ is in Kg/m^3.

A.4 Technical Specification

A.4.1 Technical Specification of Burr-Brown OPA27

SPECIFICATIONS

At V_{CC} = ±15V and T_A = +25°C, unless otherwise noted.

PARAMETER	CONDITIONS	OPA27/37G MIN	OPA27/37G TYP	OPA27/37G MAX	UNITS
INPUT NOISE[6]					
Voltage, f_O = 10Hz			3.8	8.0	nV/√Hz
f_O = 30Hz			3.3	5.6	nV/√Hz
f_O = 1kHz			3.2	4.5	nV/√Hz
f_B = 0.1Hz to 10Hz			0.09	0.25	µVp-p
Current,[1] f_O = 10Hz			1.7		pA/√Hz
f_O = 30Hz			1.0		pA/√Hz
f_O = 1kHz			0.4	0.6	pA/√Hz
OFFSET VOLTAGE[2]					
Input Offset Voltage			±25	±100	µV
Average Drift[3]	$T_{A\,MIN}$ to $T_{A\,MAX}$		±0.4	±1.8[6]	µV/°C
Long Term Stability[4]			0.4	2.0	µV/mo
Supply Rejection	±V_{CC} = 4 to 18V	94	120		dB
	±V_{CC} = 4 to 18V		±1	±20	µV/V
BIAS CURRENT					
Input Bias Current			±15	±80	nA
OFFSET CURRENT					
Input Offset Current			10	75	nA
IMPEDANCE					
Common-Mode			2 ‖ 2.5		GΩ ‖ pF
VOLTAGE RANGE					
Common-Mode Input Range		±11	±12.3		V
Common-Mode Rejection	V_{IN} = ±11VDC	100	122		dB
OPEN-LOOP VOLTAGE GAIN, DC	R_L ≥ 2kΩ	117	124		dB
	R_L ≥ 1kΩ		124		dB
FREQUENCY RESPONSE					
Gain-Bandwidth Product[5]	OPA27	5[6]	8		MHz
	OPA37	45[6]	63		MHz
Slew Rate[5]	V_O = ±10V, R_L = 2kΩ				
	OPA27, G = +1	1.7[6]	1.9		V/µs
	OPA37, G = +5	11[6]	11.9		V/µs
Settling Time, 0.01%	OPA27, G = +1		25		µs
	OPA37, G = +5		25		µs
RATED OUTPUT					
Voltage Output	R_L ≥ 2kΩ	±12	±13.8		V
	R_L ≥ 600Ω	±10	±12.8		V
Output Resistance	DC, Open Loop		70		Ω
Short Circuit Current	R_L = 0Ω		25	60[6]	mA
POWER SUPPLY					
Rated Voltage			±15		VDC
Voltage Range,					
Derated Performance		±4		±22	VDC
Current, Quiescent	I_O = 0mADC		3.3	5.7	mA
TEMPERATURE RANGE					
Specification		−40		+85	°C
Operating		−40		+85	°C

NOTES: (1) Measured with industry-standard noise test circuit (Figures 1 and 2). Due to errors introduced by this method, these current noise specifications should be used for comparison purposes only. (2) Offset voltage specification are measured with automatic test equipment after approximately 0.5 seconds from power turn-on. (3) Unnulled or nulled with 8kΩ to 20kΩ potentiometer. (4) Long-term voltage offset vs time trend line does not include warm-up drift. (5) Typical specification only on plastic package units. Slew rate varies on all units due to differing test methods. Minimum specification applies to open-loop test. (6) This parameter guaranteed by design.

A.4.2 Technical Specification of Burr-Brown INA131

SPECIFICATIONS

At T_A = +25°C, V_S = ±15V, R_L = 2kΩ, unless otherwise noted.

PARAMETER	CONDITIONS	INA131BP MIN	INA131BP TYP	INA131BP MAX	INA131AP MIN	INA131AP TYP	INA131AP MAX	UNITS
INPUT								
Offset Voltage, RTI								
Initial	T_A = +25°C		±10	±50		±25	±125	µV
vs Temperature	T_A = T_{MIN} to T_{MAX}		±0.1	±0.25		±0.25	±1	µV/°C
vs Power Supply	V_S = ±2.25V to ±18V		0.5	3		*	*	µV/V
Long-Term Stability			0.2			*		µV/mo
Impedance, Differential			10^{10} || 6			*		Ω || pF
Common-Mode			10^{10} || 6			*		Ω || pF
Input Common-Mode Range		±11	±13.5		*	*		V
Safe Input Voltage				±40			*	V
Common-Mode Rejection	V_{CM} = ±10V, ΔR_S = 1kΩ	110	120		106	110		dB
BIAS CURRENT			±0.5	±2		*	±5	nA
vs Temperature			±8			*		pA/°C
OFFSET CURRENT			±0.5	±2		*	±5	nA
vs Temperature			±8			*		pA/°C
NOISE VOLTAGE, RTI	R_S = 0Ω							
f = 10Hz			16			*		nV/√Hz
f = 100Hz			12			*		nV/√Hz
f = 1kHz			12			*		nV/√Hz
f = 10kHz			12			*		nV/√Hz
f_B = 0.1Hz to 10Hz			0.4			*		µVp-p
Noise Current								
f = 10Hz			0.4			*		pA/√Hz
f= 1kHz			0.2			*		pA/√Hz
f_B = 0.1Hz to 100Hz			18			*		pAp-p
GAIN								
Gain Error[1]			±0.01	±0.024		*	±0.1	%
Resistor Value[2]			±10	±40		*	*	%
Gain vs Temperature			±5	±10		*	±20	ppm/°C
Nonlinearity			±0.0003	±0.002		*	±0.004	% of FSR
OUTPUT								
Voltage	I_O = 5mA, T_{MIN} to T_{MAX}	±13.5	±13.7		*	*		V
	V_S = ±11.4V, R_L = 2kΩ	±10	10.5		*	*		V
	V_S = ±2.25V, R_L = 2kΩ	±1	1.5		*	*		V
Load Capacitance, max	Stable Operation		1000			*		pF
Short Circuit Current			+20/–15			*		mA
FREQUENCY RESPONSE								
Bandwidth, –3dB			70			*		kHz
Slew Rate	V_O = ±10V	0.3	0.7		*	*		V/µs
Settling Time, 0.01%			100			*		µs
Overload Recovery	50% Overdrive		20			*		µs
POWER SUPPLY								
Voltage Range		±2.25	±15	±18	*	*	*	V
Current	V_{IN} = 0V		±2.2	±3		*	*	mA
TEMPERATURE RANGE								
Specification		–40		85	*		*	°C
Operating		–40		125	*		*	°C
θ_{JA}			100			*		°C/W

* Specification same as INA131BP.

NOTES: (1) R_L = 10kΩ. (2) Absolute value of internal gain-setting resistors. (Gain depends on resistor ratios.)

A.4.3 Radio Shack Ultra -Miniature Tie Clip Microphone

Catalogue Number	33-3003
Directivity	Omnidirectional
Impedance (at 1000 Hz)	1 kOhm
Sensitivity (at 1000 Hz)	-65 dB (3 dB) (0dB=1V/micro Bar)

Appendix B

Equipment and Material Information

Table B.1 provides a partial list of equipment and materials used to conduct the research.

Table B.1: Sources of the various equipment and materials used

Material/Equipment	Source
Ceramic Honeycomb	Corning, Blacksburg USA
Laminar mass flow meters	Teleydne Electronic Technologies, Hampton VA, USA
Thermal mass flow meters	Eldridge Products Inc., Monterey CA, USA
Tie-clip miniature microphones	Radio Shack, Fort worth TX, USA
Hotwire anemometer	AA Labs, Israel
ICCD camera	Stanford Computer Optics Inc., Palo Alto CA, USA
Photo-multiplier tube	Hammatsu Photonics, Japan
$5\frac{1}{4}$, 60 Watt, 8 Ohm Speaker	MCM Audio
$6\frac{1}{2}$, 160 Watt, 8 Ohm Speaker	DynaVox

Appendix C

Error Analysis

C.1 Errors in Dynamic Velocity Measurement

Due to the fact that the derivative in equation A.10 has been replaced by a finite difference approximation and the instruments have limitations to their accuracy, the following errors are inherent in the velocity measurement using a two microphone technique.

a. Finite difference approximation error
b. Difference in microphone sensitivity
c. Phase mismatch error
d. Near field effects

The spatial gradient at the midpoint between the two microphones was approximated as

$$\frac{\partial P}{\partial x} \approx \frac{P_2 - P_1}{\Delta\, x} \tag{C.1}$$

where $\Delta\, x$ was 50 mm. Waser et al. [72] have analyzed the error due to this finite difference approximation with $\Delta x = 50$ mm and have noted that the error increases with increase in the excitation frequency. For $\Delta x = 50$ mm and the frequency of 630 Hz, the error in the magnitude of the measurement is less than 0.5 dB. Therefore, for the present research, the maximum finite difference error is considered to be ± 0.5 dB.

Table C.1: Maximum errors in the fuel flow rates

Fuel	Maximum error
Methane	± 0.25 cc/sec
Propane	± 0.129 cc/sec
Ethane	± 0.203 cc/sec

Since the two microphones used were not perfectly identical, they were calibrated to the same acoustic source as described in Chapter 5 and Chapter 9. The calibration indicated a maximum error in magnitude of ±0.5 dB and a maximum error in phase of ±0.5 degrees. As within the combustor the phase of the generated standing wave does not vary spatially, the measured phase error was the total phase mismatch error. Since the microphones were far away from the speaker and the wave front was shown to be truly planar at the point of measurement, the error due to near field effects was not applicable and thus, neglected.

Therefore, the maximum error in the magnitude of the dynamic velocity measurement was ±1 dB, while the maximum error in the phase of the velocity measurement was ±0.5 degrees.

C.2 Errors in Flow Controllers

The main source of error generated in the display of the readings of the flow meters is due to the uncertainty in its calibration. A number of flow meters were used in the research detailed in this document. They have been listed in Appendix B and their maximum errors are reported here.

The Hastings mass flow meters used in the laminar flame dynamic experiments were factory calibrated. The air mass flow meter was built for a maximum flow rate of 25 slpm, while the fuel mass flow meter was built for a maximum methane flow rate of 1.5 slpm. The flow meters are rated to be accurate within 1 % of the full scale, which results in the total uncertainty of the air flow meter to be within ±4.17 cc/sec, while the maximum uncertainty in the flow rates of the three fuels used are shown in Table C.1.

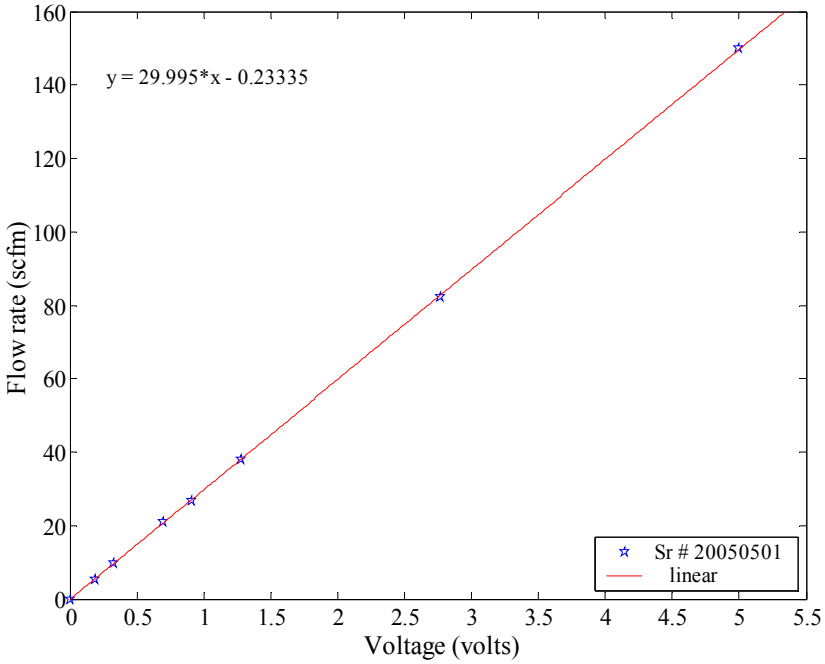

Figure C.1: Calibration of the flow meter, SR No. 20050501

The fuel flow for the turbulent swirl stabilized flame dynamic experiment was measured using a Hastings flow meter, which was rated for a maximum flow of 1.5 scfm of methane and was factory calibrated with a maximum uncertainty of 1 % of full scale reading. Therefore, the maximum error in the fuel flow measurement was calculated to be ± 0.015 scfm.

The air flow meters used for the measurement of the axial and the tangential air flow in the turbulent flame dynamic experiment were built for a maximum flow rate of 150 scfm and were factory calibrated. Linear calibration equations were generated from the calibration data provided by the manufacturer. The comparison of the data and the equations for the two flow meters are shown in Figure C.1 and Figure C.2. The error associated with using the calibration equations was computed by performing a simple regression analysis on the data using a statistical analysis program [90]. The program calculated a 95 % confidence interval to lie between $\pm$ 0.16 % of the full scale for both the calibration equations. Therefore, within a flow rate range of 0-25 scfm, the error range associated with both the air flow meters was

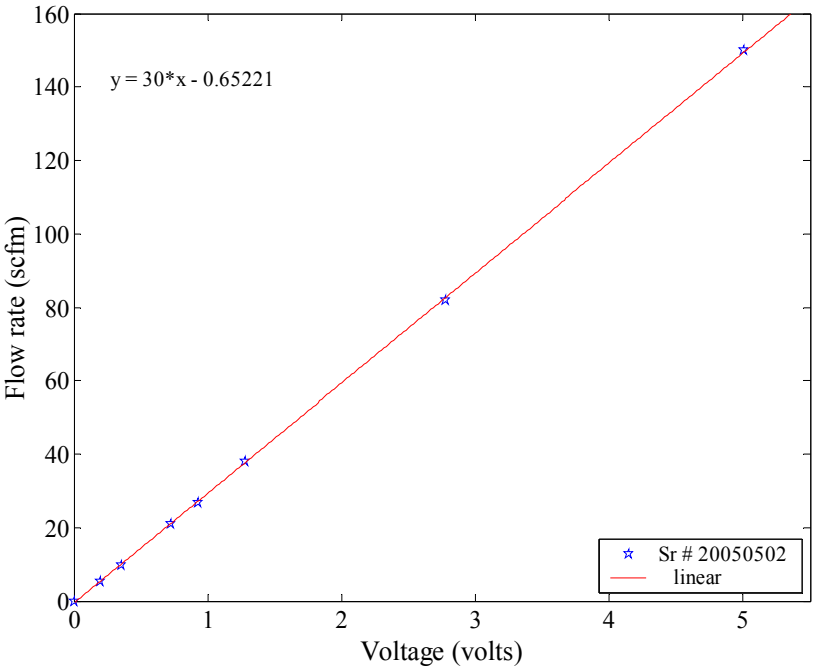

Figure C.2: Calibration of the flow meter, SR No. 20050502

$\pm$ 0.24 scfm.

C.3 Chemiluminescence

The chemiluminescence signal was captured using the optical collecting system and was transmitted by a fiber optic cable. The signal was then filtered using a monochrometer and finally sensed by a PMT. Each of these components have their own efficiencies due to which certain amount of captured light is lost. Furthermore, there are uncertainties associated with the measurement of the OH^* signal and conversion of the signal to voltage. Based on repeated measurements of a given signal, the author has noted that all the uncertainties combined produced a maximum error in the OH^* measurement of $\pm$ 0.25 dBV. For calibration of the OH^* signal, the reader is referred to work by Haber [70].

Appendix D

Experimental Data

This appendix lists the model parameters generated by fitting the experimental data for both the laminar and turbulent flame dynamics. The experimentally measured honeycomb temperatures along with the computed flame temperatures for laminar flame dynamic experiments are also detailed here.

Table D.1: Poles, zeros, gain and time delay for burner stabilized laminar flat flame burning methane

Total Flow Q_{Total} cc/sec	Equivalence Ratio (Φ)	Poles Hz	Zeros Hz	Gain	Time Delay seconds
145	0.5	-1.46 $\pm$27.37 -0.1275 $\pm$23.39	-0.675 $\pm$23.15 -123.83 $\pm$302.79	3.236 $\times 10^{-2}$	1.68 $\times 10^{-3}$
145	0.55	-17.54 $\pm$33.64 -7.32 $\pm$43.31	-9.70 -50.32 -825.83 -17552.95	4.756 $\times 10^{-4}$	1.10 $\times 10^{-3}$

Table D.1: (continued)

Total Flow Q_{Total} cc/sec	Equivalence Ratio (Φ)	Poles Hz	Zeros Hz	Gain	Time Delay seconds
145	0.6	-12.28 ±27.64 -27.76 ±76.19	-11.91 -51.54 -676.31 ±903.39	1.307 $\times 10^{-2}$	9.00 $\times 10^{-4}$
145	0.65	-11.97 ±30.87 -47.21 ±97.87	-16.77 -52.67 -977.91 39305.19	-7.083 $\times 10^{-4}$	8.20 $\times 10^{-4}$
145	0.75	-14.75 ±37.20 -124.36 ±129.27	-13.65 -72.89 -260.12 ±830.93	1.045 $\times 10^{-1}$	7.50 $\times 10^{-4}$
160	0.5	-3.65 ±34.44 -11.98 ±38.53	-18.84 ±19.84 -469.83 ±415.93	1.536 $\times 10^{-2}$	1.35 $\times 10^{-3}$
160	0.55	-8.89 ±28.92 -24.96 ±69.79	-14.98 -28.28 -215.16 ±351.65	9.518 $\times 10^{-2}$	1.30 $\times 10^{-3}$
160	0.6	-10.41 ±30.00 -58.01 ±98.02	-12.92 -39.55 -177.36 ±388.27	2.043 $\times 10^{-1}$	1.15 $\times 10^{-3}$
160	0.65	-13.25 ±28.54 -97.41 ±124.05	-10.05 -60.27 -195.28 ±387.66	3.306 $\times 10^{-1}$	1.10 $\times 10^{-3}$

Table D.1: (continued)

Total Flow Q_{Total} cc/sec	Equivalence Ratio (Φ)	Poles Hz	Zeros Hz	Gain	Time Delay seconds
160	0.75	-19.52 ±25.76 -166.06 ±176.76	-4.45 -124.70 -193.63 ±6.55.28	2.329×10^{-1}	7.50×10^{-4}
180	0.5	-10.82 ±27.08 -13.03 ±51.56	-26.45 ±6.27 -509.49 ±445.36	1.766×10^{-2}	1.25×10^{-3}
180	0.55	-12.69 ±23.24 -40.83 ±98.81	-4.08 -80.60 -605.73 ±537.78	3.729×10^{-2}	9.00×10^{-4}
180	0.6	-12.90 ±21.15 -95.54 ±132.02	-5.40 -80.03 -456.66 ±804.71	7.021×10^{-2}	7.50×10^{-4}
180	0.65	-14.93 ±23.66 -134.24 ±168.76	-6.53 -100.30 126.52 ±784.39	1.433×10^{-1}	4.90×10^{-4}
180	0.75	-19.01 ±21.65 -161.93 ±213.95	-1.37 -198.63 -651.57 ±4418.21	5.068×10^{-3}	4.00×10^{-4}
200	0.5	-13.16 ±35.46 -15.70 ±59.15	-21.89 -37.70 -447.47 ±560.66	2.450×10^{-2}	1.03×10^{-3}

Table D.1: (continued)

Total Flow Q_{Total} cc/sec	Equivalence Ratio (Φ)	Poles Hz	Zeros Hz	Gain	Time Delay seconds
200	0.55	-13.01 $\pm$30.57 -66.97 $\pm$117.03	-13.59 -57.59 -252.33 $\pm$446.05	9.235 $\times 10^{-2}$	9.40 $\times 10^{-4}$
200	0.6	-13.93 $\pm$23.06 -145.69 $\pm$167.03	-3.29 -87.56 -197.59 $\pm$498.16	4.193 $\times 10^{-1}$	9.21 $\times 10^{-4}$
200	0.65	-14.81 $\pm$20.47 -192.76 $\pm$199.06	-3.31 -106.52 -149.42 $\pm$590.59	4.480 $\times 10^{-1}$	7.54 $\times 10^{-4}$
200	0.75	-19.34 $\pm$27.56 -164.09 $\pm$240.54	-2.38 -282.06 1430.45 $\pm$634.14	4.100 $\times 10^{-2}$	1.00 $\times 10^{-4}$

Table D.2: Poles, zeros, gain and time delay for burner stabilized laminar flat flame burning propane

Total Flow Q_{Total} cc/sec	Equivalence Ratio (Φ)	Poles Hz	Zeros Hz	Gain	Time Delay seconds
145	0.55	-7.41 $\pm$45.84 -12.92 $\pm$67.50	-21.74 -62.72 -218.62 5015.41	-1.165 $\times 10^{-2}$	1.050 $\times 10^{-3}$
145	0.60	-10.97 $\pm$38.87 -36.57 $\pm$98.82	-14.68 -61.77 -664.48 3693.48	-1.255 $\times 10^{-2}$	7.20 $\times 10^{-4}$
145	0.65	-10.80 $\pm$38.92 -87.18 $\pm$115.98	-498.62 $\pm$737.57 -32.28 $\pm$87.96	9.069 $\times 10^{-2}$	7.18 $\times 10^{-4}$
145	0.75	-14.54 $\pm$35.82 -123.59 $\pm$168.83	-6.39 -231.10 -341.73 -2670.29	6.778 $\times 10^{-2}$	7.000 $\times 10^{-4}$
160	0.55	-7.71 $\pm$41.13 -12.93 $\pm$72.16	-20.025 -55.19 -404.74 -2061.55	1.945 $\times 10^{-2}$	9.50 $\times 10^{-4}$

Table D.2: (continued)

Total Flow Q_{Total} cc/sec	Equivalence Ratio (Φ)	Poles Hz	Zeros Hz	Gain	Time Delay seconds
160	0.6	-11.84 ±40.16 -40.46 ±103.85	-14.26 -82.78 -574.01 ±486.62	6.288 $\times 10^{-2}$	8.50 $\times 10^{-4}$
160	0.65	-13.72 ±34.83 -89.31 ±124.60	-11.64 -83.05 -444.32 ±493.86	1.678 $\times 10^{-1}$	8.10 $\times 10^{-4}$
160	0.75	-14.71 ±34.60 -158.88 ±167.34	-5.60 -149.52 -347.45 ±527.82	3.189 $\times 10^{-1}$	7.770 $\times 10^{-1}$
180	0.52	-9.80 ±43.83 -9.57 ±74.43	-29.12 -47.78 -490.25 11683.27	-3.513 $\times 10^{-3}$	9.10 $\times 10^{-4}$
180	0.55	-15.23 ±37.33 -21.28 ±95.18	-21.03 -66.24 -475.91 ±449.46	6.622 $\times 10^{-2}$	9.00 $\times 10^{-4}$
180	0.60	-18.54 ±26.73 -79.80 ±134.12	-8.02 -107.59 -566.81 7039.52	-1.719 $\times 10^{-2}$	7.00 $\times 10^{-4}$

Table D.2: (continued)

Total Flow Q_{Total} cc/sec	Equivalence Ratio (Φ)	Poles Hz	Zeros Hz	Gain	Time Delay seconds
180	0.65	-17.74 ±31.59 -124.08 ±156.74	-9.51 -101.72 -834.08 ± 881.60	7.870 $\times 10^{-2}$	6.50 $\times 10^{-4}$
180	0.75	-18.54 ±20.97 -157.51 ±180.18	-0.787 -158.25 -1045.71 -4753.03	2.851 $\times 10^{-2}$	4.80 $\times 10^{-4}$
200	0.52	-12.25 ±46.06 -14.20 ±86.63	-26.55 -66.53 -625.94 3681.57	-1.229 $\times 10^{-2}$	8.00 $\times 10^{-4}$
200	0.55	-14.89 ±40.92 -25.06 ±100.85	-16.42 -88.27 -960.02 ±272.10	3.383 $\times 10^{-2}$	9.40 $\times 10^{-4}$
200	0.60	-18.57 ±30.60 -78.53 ±157.07	-9.48 -117.81 -353.47 ±498.57	2.342 $\times 10^{-1}$	8.015 $\times 10^{-4}$
200	0.65	-16.93 ±28.11 -130.68 ±199.79	-2.03 -146.05 -245.07 ±426.36	6.215 $\times 10^{-1}$	8.600 $\times 10^{-4}$

Table D.2: (continued)

Total Flow Q_{Total} cc/sec	Equivalence Ratio (Φ)	Poles Hz	Zeros Hz	Gain	Time Delay seconds
200	0.75	-15.73 $\pm$30.05 -180.50 $\pm$183.99	-3.22 -131.06 -161.46 $\pm$843.01	3.046 $\times 10^{-1}$	5.250 $\times 10^{-4}$

Table D.3: Poles, zeros, gain and time delay for burner stabilized laminar flat flame burning ethane

Total Flow Q_{Total} cc/sec	Equivalence Ratio (Φ)	Poles Hz	Zeros Hz	Gain	Time Delay seconds
145	0.6	-7.39 $\pm$43.15 -25.17 $\pm$74.09	-23.09 -45.61 -311.73 2014.24	-1.904 $\times 10^{-2}$	9.50 $\times 10^{-4}$
145	0.65	-7.34 $\pm$39.96 -48.01 $\pm$81.47	-21.34 $\pm$23.71 275.23 $\pm$967.14	2.672 $\times 10^{-2}$	4.50 $\times 10^{-4}$
145	0.75	-13.49 $\pm$37.63 -95.06 $\pm$165.15	-9.71 -179.59 $\pm$143.80 -1698.20	7.993 $\times 10^{-2}$	7.50 $\times 10^{-4}$
160	0.55	-11.53 $\pm$39.62 -2.45 $\pm$48.06	-19.74 $\pm$17.89 -478.27 1549.53	-8.535 $\times 10^{-3}$	1.00 $\times 10^{-3}$?
160	0.6	-8.998 $\pm$41.93 -32.89 $\pm$81.57	-28.04 $\pm$16.07 1185.89 -2601.98	-6.591 $\times 10^{-3}$	5.00 $\times 10^{-4}$
160	0.65	-12.79 $\pm$37.97 -69.09 $\pm$105.07	-17.55 -60.72 -601.53 $\pm$642.08	4.884 $\times 10^{-2}$	7.50 $\times 10^{-4}$

Table D.3: (continued)

Total Flow Q_{Total} cc/sec	Equivalence Ratio (Φ)	Poles Hz	Zeros Hz	Gain	Time Delay seconds
160	0.75	-14.29 $\pm$35.35 -129.02 $\pm$173.11	-6.86 -214.69 -442.13 -1252.79	8.984 $\times 10^{-2}$	7.00 $\times 10^{-4}$
180	0.55	-11.71 $\pm$37.79 -10.39 $\pm$59.04	-27.53 $\pm$12.80 -1244.97 2650.76	-3.103 $\times 10^{-3}$	7.70 $\times 10^{-4}$
180	0.6	-14.04 $\pm$33.75 -39.17 $\pm$98.80	-24.30 -45.66 -603.08 -39536.54	1.157 $\times 10^{-3}$	6.80 $\times 10^{-4}$
180	0.65	-16.98 $\pm$34.14 -82.98 $\pm$127.03	-13.02 -104.10 -402.18 -2240.04	5.283 $\times 10^{-2}$	6.80 $\times 10^{-4}$
180	0.75	-14.43 $\pm$30.65 -103.97 $\pm$177.23	-6.63 -187.60 $\pm$119.17 35335.57	-6.256 $\times 10^{-3}$	5.50 $\times 10^{-4}$
200	0.55	-12.44 $\pm$42.66 -8.96 $\pm$60.28	-24.59 $\pm$18.61 824.63 -1109.45	-1.399 $\times 10^{-2}$	7.00 $\times 10^{-4}$

Table D.3: (continued)

Total Flow Q_{Total} cc/sec	Equivalence Ratio (Φ)	Poles Hz	Zeros Hz	Gain	Time Delay seconds
200	0.6	-18.58 $\pm$33.52 -46.78 $\pm$123.67	-12.80 -165.96 -266.52 4152.43	-2.132 $\times 10^{-2}$	6.35 $\times 10^{-4}$
200	0.65	-17.02 $\pm$35.23 -92.16 $\pm$144.77	-11.55 -130.39 -479.29 -1851.50	6.226 $\times 10^{-2}$	7.00 $\times 10^{-4}$
200	0.75	-16.87 $\pm$31.27 -94.50 $\pm$199.31	-3.09 -169.58 $\pm$180.04 1149.56	-2.067 $\times 10^{-1}$	4.50 $\times 10^{-4}$

Table D.4: Temperatures measured at the top and bottom surface of the honeycomb for experiments burning methane

Total Flow Q_{Total} cc/sec	Equivalence Ratio (Φ)	Top Surface Temperature Kelvin	Bottom Surface Temperature Kelvin
145	0.5	641.28	328.16
145	0.55	798.61	340.23
145	0.6	902.6	347.94
145	0.65	958.51	354.19
145	0.75	1064.21	365.52
160	0.5	733.17	332.75
160	0.55	865.79	341.67
160	0.6	958.51	345.53
160	0.65	1015.66	355.64
160	0.75	1095	358.53
180	0.5	780.37	326.95
180	0.55	893.89	332.99
180	0.6	994.8	341.43
180	0.65	1043.75	345.29
180	0.75	1134.6	351.58
200	0.5	789.51	323.8
200	0.55	913.02	326.95
200	0.6	1024.79	330.1
200	0.65	1059.32	333.24
200	0.75	1161.01	276.05

Table D.5: Temperatures measured at the top and bottom surface of the honeycomb for experiments burning propane

Total Flow Q_{Total} cc/sec	Equivalence Ratio (Φ)	Top Surface Temperature Kelvin	Bottom Surface Temperature Kelvin
145	0.55	856.06	336.13
145	0.60	926.84	343.12
145	0.65	997.31	345.05
145	0.75	1102.24	354.92
160	0.55	839.15	332.27
160	0.60	938.87	340.47
160	0.65	1016.49	345.05
160	0.75	1115.86	354.43
180	0.52	799.52	321.13
180	0.55	859.6	327.92
180	0.60	977.14	335.41
180	0.65	1032.23	329.85
180	0.75	1143.67	340.71
200	0.50	799.52	317.49
200	0.55	882.51	321.38
200	0.60	922.84	325.01
200	0.65	1039.64	329.13
200	0.75	1161.8	334.44

Table D.6: Temperatures measured at the top and bottom surface of the honeycomb for experiments burning ethane

Total Flow Q_{Total} cc/sec	Equivalence Ratio (Φ)	Top Surface Temperature Kelvin	Bottom Surface Temperature Kelvin
145	0.60	836.47	332.27
145	0.65	903.47	339.99
145	0.75	1009.84	346.49
160	0.55	756.44	325.98
160	0.60	861.37	331.54
160	0.65	937.16	338.06
160	0.75	1038.82	340.71
180	0.55	738.78	315.3
180	0.60	878.12	323.32
180	0.65	944.01	327.44
180	0.75	1060.95	327.44
200	0.55	751.8	316.27
200	0.60	874.61	315.3
200	0.65	959.36	323.08
200	0.75	1081.27	328.4

Table D.7: Flame temperature for burner stabilized laminar flat flame

Total Flow Q_{Total} cc/sec	Equivalence Ratio (Φ)	Flame Temperature		
		Methane Kelvin	Propane Kelvin	Ethane Kelvin
145	0.5	1462		
145	0.55	1484	1476	
145	0.6	1503	1499	1494
145	0.65	1522	1515	1501
145	0.75	1566	1552	1546
160	0.5	1475		
160	0.55	1498	1488	1476
160	0.6	1518	1508	1500
160	0.65	1539	1527	1517
160	0.75	1584	1568	1566
180	0.5	1484		
180	0.52		1490	
180	0.55	1516	1507	1490
180	0.6	1537	1525	1519
180	0.65	1559	1546	1539
180	0.75	1607	1593	1592
200	0.5	1512		
200	0.52		1505	
200	0.55	1533	1517	1492
200	0.6	1555	1546	1536
200	0.65	1577	1562	1547
200	75	1627	1617	1614

Table D.8: Poles, zeros, gain and time delay for swirl stabilized turbulent flame burning methane

Total Flow Q_{Total} cc/sec	Swirl number S	Equivalence Ratio (Φ)	Poles Hz	Zeros Hz	Gain
15	0.55	0.79	-29.90 $\pm$110.66 -22.72 $\pm$67.29 -10.00 $\pm$30.65 -3.14 $\pm$28.93	20.51 $\pm$146.30 59.21 $\pm$72.88 -51.60 -1.93 $\pm$29.78 -1.93 $\pm$29.78 -1.198	-3.398 $\times 10^{-3}$
15	0.55	1.19	-28.98 $\pm$112.09 -25.65 $\pm$52.78 -0.436 $\pm$37.43 -10.02 $\pm$14.20	11.03 $\pm$148.77 54.74 $\pm$88.25 -0.423 $\pm$37.57 12.03 -3.516	-6.577 $\times 10^{-3}$
15	0.60	0.79	-3.57 $\pm$104.42 -22.07 $\pm$96.15 -2.56 $\pm$60.60 -37.8 -6.08	43.15 $\pm$127.77 -3.26 $\pm$103.25 -2.70 $\pm$60.11 33.1 -4.11	-3.151 $\times 10^{-2}$

Table D.8: (continued)

Total Flow Q_{Total} cc/sec	Swirl number S	Equivalence Ratio (Φ)	Poles Hz	Zeros Hz	Gain
15	0.60	1.19	-30.84 ±132.29 -22.34 ±73.48 -8.27 ±53.48 -11.5 -5.39	557 45.98 ±157.63 58.7 -8.15 ±55.86 -39.2 1.90	2.989 $\times 10^{-3}$
15	0.65	0.79	-24.14 ±177.66 -1.20 ±138.30 -24.64 ±102.90 -58.3 -9.74	-68.94 ±321.40 68.17 ±178.24 -1.49 ±138.51 113 -2.77	-2.848 $\times 10^{-3}$
15	0.65	1.19	-30.22 ±196.69 -1.28 ±157.29 -32.31 ±111.49 -70.6 -13.3	-335 28.93 ±225.08 113.69 ±111.77 -2.01 ±157.59 -0.522	6.500 $\times 10^{-3}$
20	0.55	0.79	-0.575 ±118.51 -27.07 ±104.41 -22.86 ±48.23 -7.99 ±58.10	37.76 +153.32 -0.451 ±117.42 43.70 ±48.90 4.50 ±5.34	9.637$\times 10^{-3}$

Table D.8: (continued)

Total Flow Q_{Total} cc/sec	Swirl number S	Equivalence Ratio (Φ)	Poles Hz	Zeros Hz	Gain
20	0.55	1.19	-25.90 ±100.32 -3.31 ±88.64 -12.62 ±54.20 -12.18 ±34.85	18700 50.26 ±109.29 -3.27 ±89.39 -15.09 ±44.14 -2.43	5.070 $\times 10^{-5}$
20	0.60	0.79	-7.90 ±131.62 -26.29 ±94.02 -20.10 ±28.03 -8.94 $\times 10^{-2}$ ±13.89	-12.37 ±132.32 51.38 ±125.87 51.4 -6.47 +19.52 -2.36	-1.890 $\times 10^{-2}$
20	0.60	1.19	-0.66 ±140.88 -38.94 ±127.22 -33.43 ±61.60 -7.64 ±14.53	1800 131.65 ±160.35 -0.875 ±140.64 123 -2.78 ±13.41	4.450 $\times 10^{-4}$
20	0.65	0.79	-31.78 ±127.08 -75.6 -4.47 $\times 10^{-2}$ ±66.56 -3.65 ±21.32 -6.91	79.88 ±170.09 92.1 -3.07 $\times 10^{-2}$ ±66.56 -3.26 ±22.85 -0.346	-2.580 $\times 10^{-2}$

Table D.8: (continued)

Total Flow Q_{Total} cc/sec	Swirl number S	Equivalence Ratio (Φ)	Poles Hz	Zeros Hz	Gain
20	0.65	1.19	-97.2 -0.803 $\pm$135.62 -33.63 $\pm$111.81 -0.415$\pm$106.21 -8.26	74.38 +151.46 95.2 -1.01 $\pm$135.15 -0.278$\pm$106.16 -2.00	-2.902 $\times 10^{-2}$

Appendix E

High Pressure Combustor-Preliminary Design

Preliminary design of a 10 bar, 1.5 megawatt gaseous swirl stabilized combustor is described in this section. Figure E.1 shows a schematic of the combustor. The primary objective to design this combustor was the need to study the various aspects of thermo-acoustic instabilities and their control in a gaseous lean premixed combustion environment. The combustor was designed for a maximum flow rate of 0.55 Kg/sec, a maximum operating pressure of 10 bar, and a maximum inlet air temperature of 840 K. It was expected to maintain a fully premixed swirl stabilized flame using natural gas as fuel. The combustor was jacketed with cold pressurized air from the compressor, to cool the combustor walls. This simulated the back cooled liners of modern land based gas turbines. To gain optical access to the reaction zone, the combustor was conceptualized to be of 200 mm $\times$ 200 mm square cross section. The side walls were designed to house windows of high temperature quartz, which could easily be replaced with metallic walls to enable the housing of various sensors. The combustor was designed to behave as a Helmholtz resonator. Different plugs having different combination of inner diameter and length could be used to excite different acoustic frequencies. The fuel nozzles injecting natural gas into the swirling air were designed to be choked, while the exhaust downstream of the combustor was quenched with water spray to a temperature of about 600 K.

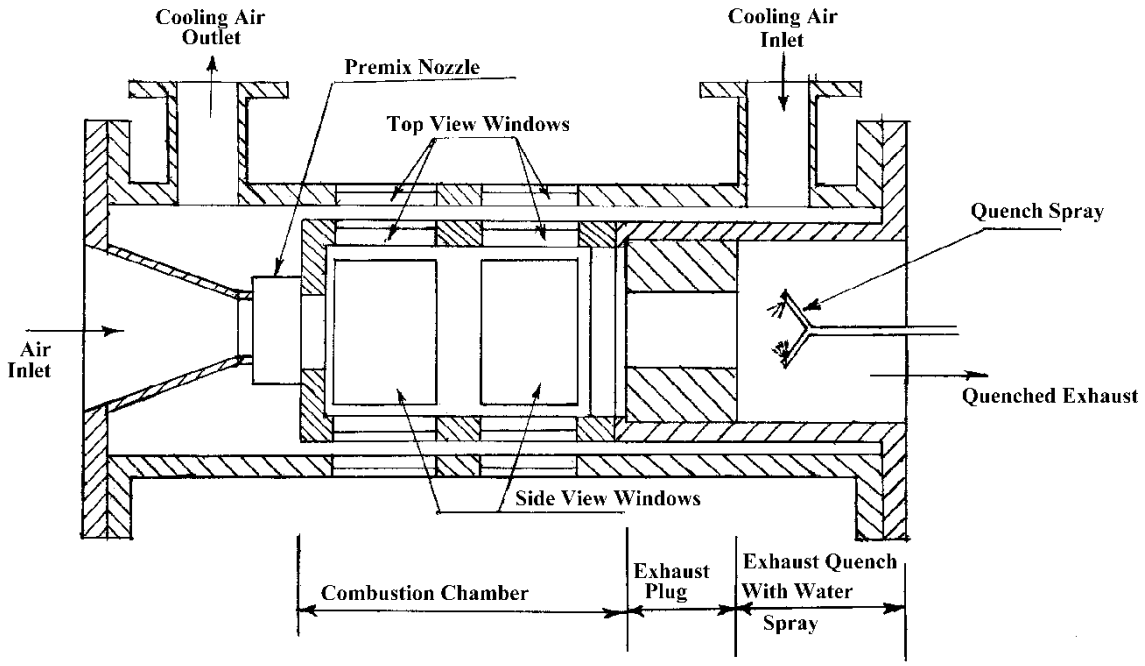

Figure E.1: Sketch of the high pressure combustor

A numerical code was written in visual basic to simulate the steady heat transfer within the combustor so as to obtain a reasonable estimate of the wall temperatures and the energy losses. The simulation was based on the following assumptions:

(1) Flow entered the combustor at the adiabatic flame temperature.
(2) The radiation calculation assumed surfaces and the gases to be diffuse.
(3) One-dimensional analysis.

The combustor was broken into different elements and solved for the energy balance including conductive, convective and radiative heat transfer modes. The radiation exchange between gas and the combustor walls was estimated based on the average wall and gas temperature inside the entire combustor and was based on the mean beam length approximation detailed by Howell [91]. First, the convective and the conductive modes were solved to obtain the initial solution, which was then refined by incorporating the radiative heat transfer

mode.

The following equations were used by the convective heat transfer in the solution

$$Pr = \frac{\mu C_p}{k} \tag{E.1}$$

$$Re = \frac{\rho U D_h}{\mu} \tag{E.2}$$

$$C_f = [1.82 \log(Re) - 1.62]^{-2} \tag{E.3}$$

$$Nu_x = \frac{C_f}{8} \frac{Re\, Pr}{1.07 + 12.7\{(\frac{C_f}{8})^{\frac{1}{2}} [Pr^{\frac{2}{3}} - 1]\}} \tag{E.4}$$

$$h_x = \frac{Nu_x k}{D_h} \tag{E.5}$$

where Pr is the Prandtl number, C_f is the friction coefficient, Re is the Reynolds number, Nu_x is the Nusselts number.

For radiation calculations, the following correlations were used

$$Le = \frac{3.4\,(volume\ of\ combustor)}{(Surface\ area\ of\ combustor)} \tag{E.6}$$

$$M_R = \left\{ \frac{Fuel}{Air} \right\}_{mass} \tag{E.7}$$

$$\epsilon_g = 1 - exp\left\{ -290\, P\, (Le\ M_r)^{\frac{1}{2}}\ T_g^{-\frac{3}{2}} \right\} \tag{E.8}$$

$$\alpha_g = \epsilon_g \left\{ \frac{T_g}{T_w} \right\}^{\frac{3}{2}} \tag{E.9}$$

The details of the corelation for ϵ_g and α_g are detailed in "Gas Turbine Combustion" by Lefebvre [92].

Appendix F

Effects of Probe Signal on the Heat Release Dynamics

Vaudrey et al. [93] have developed and implemented different control algorithms to control the thermo-acoustic instability in the Rijke tube described in Chapter 6, Section 6.2.4. In this process it was noted that the presence of a probe signal at a low frequency (40-130 Hz) helped immensely in stabilizing the thermo-acoustic instability occurring at 178 Hz. To investigate this phenomenon, experiments were conducted on the laminar flat flame burner described in Chapter 4, for $Q_{Total} = 146$ cc/sec and two equivalence ratios of $\Phi = 0.73$ and $\Phi = 0.61$. A constant voltage of 100 mV was applied to the speaker at 170 Hz. This ensured a linear dynamic response from the flame as measured by the OH^* signal. Experiments were conducted by monotonically increasing the voltage applied at the probe frequency which was lower than 170 Hz and measuring the dynamic OH^* chemiluminescence at 170 Hz. For experiments with $\Phi = 0.61$, the probe frequency was chosen to be 130 Hz, while for condition with $\Phi = 0.73$, the probe signal was taken to be 70Hz. Figure F.1 shows the results of the experiment. Here, the magnitude of the dynamic OH^* chemiluminescence signal, a measure of the dynamic heat release rate has been plotted as a function of probe signal.

For both the experiments, it is observed that the dynamic heat release rate drops with increase in probe voltage. However, the decrease is non-linear in nature. Although, a fourth order polynomial perfectly fits both the data sets, the behavior of the response for increases

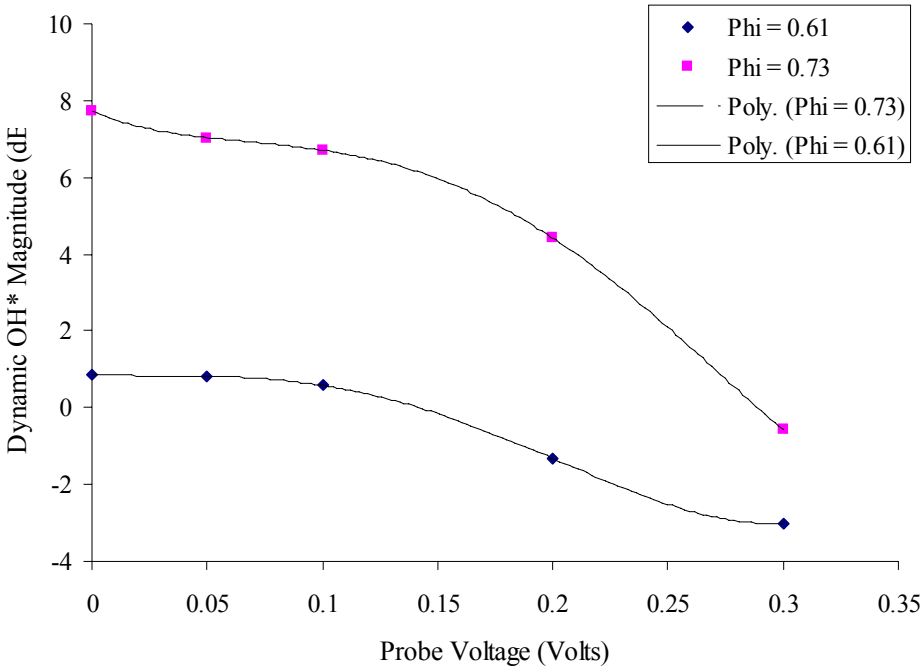

Figure F.1: The dependence of the dynamic OH* signal measured at 170 Hz on the voltage applied at the probe frequency

in probe voltage is quite different. The author believes that this phenomenon is related to enhanced heat transfer from the flame to the honeycomb and to the combustor walls. Through an increase in the dynamic heat losses from the flame, the enthalpy of the gases in the flame is reduced. Thus, the flame temperature is lower leading to lower dynamic OH^* chemiluminescence signal. This is schematically shown in Figure F.2. Here, q' is the part of the total chemical energy that is utilized for adding sensible enthalpy to the products of combustion and it is this portion of the chemical energy that couples with the acoustics. q'_{Loss} is the dynamic component of the chemical energy that is lost to the environment, while q'_{rec} is the fraction that is re-circulated via the honeycomb.

Due to the fourth order dependence seen in Figure F.1, the author is inclined to believe that radiative heat transfer is the dominant mode. However, the effects of the unsteady convective heat transfer in a developing boundary layer just downstream of the flame cannot be ruled out. The exact mechanism and its effective range can only be deduced by developing

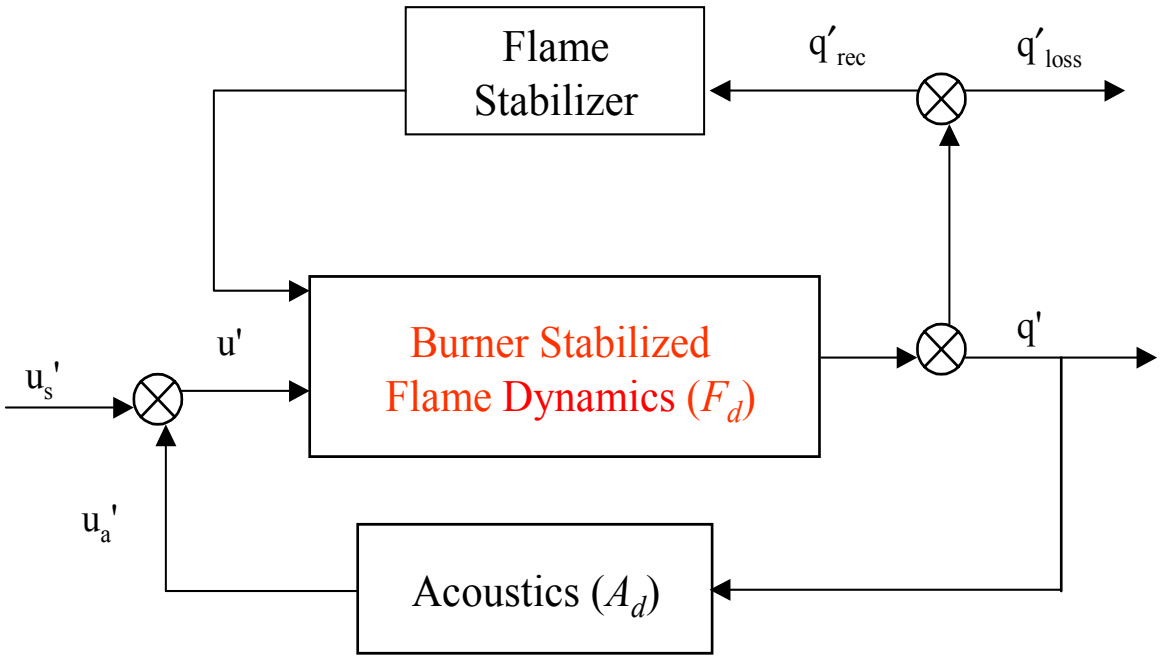

Figure F.2: Systems level block diagram describing the dynamic process involved in the probe signal experiment

the detailed physics based dynamic model for the laminar flat flame burner, as proposed in Chapter 12, Section 12.1.1.

A similar experiment was conducted on the swirl stabilized turbulent combustor. However, no significant decrease in the dynamic OH^* chemiluminescence was observed. The decrease recorded was in the range of 1 to 2 dBV. Based on the theory that this phenomenon is related to heat transfer oscillations within the combustor, one would not expect the probe signal to have any effect on the flame dynamics of turbulent flames, because due to the high turbulence present, the convective heat transfer is already enhanced and small u' perturbations are not expected to generate any significant perturbation in the flame temperature to enhance the radiative mode. However, the author expects that if the experiment is carried out with low frequency pulses of fuel, the phenomenon might become prominent in turbulent flames.

Appendix G

Dimensioned Drawing of Swirl Stabilized Turbulent Combustor

Figure G.1 shows the dimensioned drawing of the swirl stabilized turbulent combustor. For detailed part drawings please contact the author or the committee chair Dr. Uri Vandsburger.

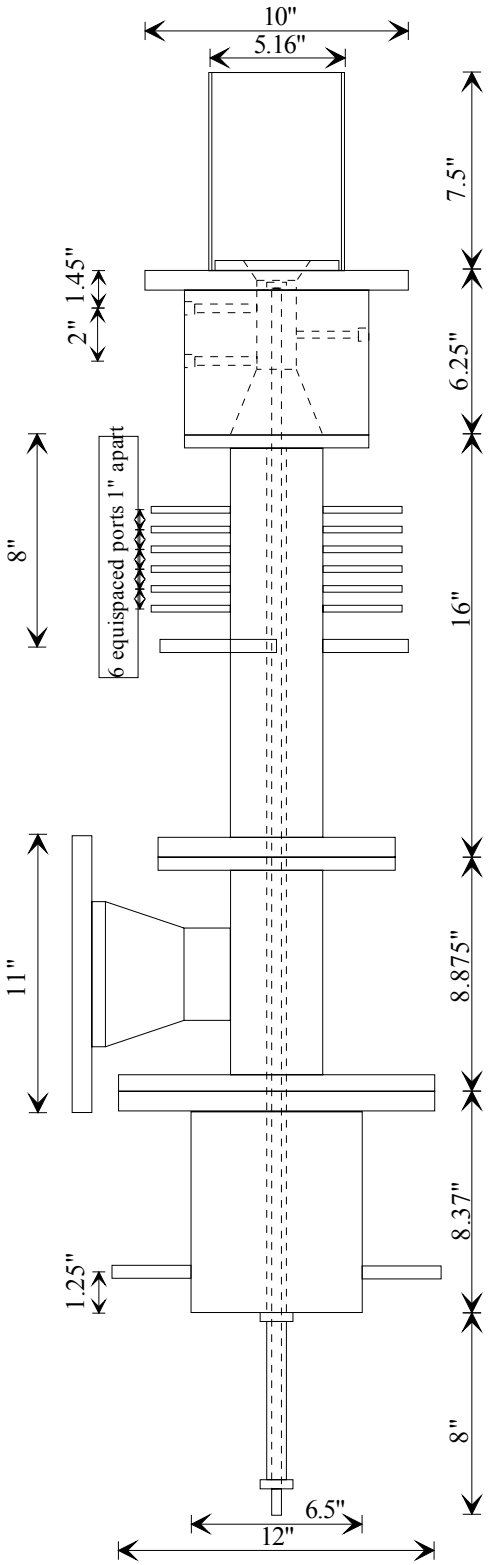

Figure G.1: Dimensioned Drawing of Swirl Stabilized Turbulent Combustor

Bibliography

[1] S. Kakac, R. K. Shah, and W Aung. *Handbook of Single Phase Convective Heat Transfer*. John Wiley and Sons, 1987.

[2] J. Tyndall. *Sound*. D. Appleton and Company, NY, 1897.

[3] Lord Rayleigh. The explanation of certain acoustical phenomena. *Royal Institution Proceedings, 8: 536-542*, 1878.

[4] C. A. Fannin. *Linear Modeling and Analysis of Thermoacoustic Instabilities in a Gas Turbine Combustor*. PhD thesis, Virginia Polytechnic Institute and State University, Blacksburg, Virginia, July 2000.

[5] U. Kruger, J. Hüren, S. Hoffmann, W. Krebs, and D. Bohn. Prediction of thermoacoustic instabilities with focus on the dynamic flame behavior for the 3A-Series gas turbine of siemens kwu. *The International Gas Turbine and Aeroengine Congress, Indianapolis, USA, ASME*, (99-GT-111), June 1999.

[6] P. J. M. Cronemyr, C. J. Hulme, and C. Troger. Coupled acoustic-structure analysis of an annular dle combustor. *The International Gas Turbine and Aeroengine Congress, Stockholm, Sweden, ASME*, (98-GT-502), June 1998.

[7] M. Fleifil, A.M. Annaswamy, Z. A. Goneim, and A. F. Ghoniem. Response of a laminar premixed flame to flow oscillations: A kinematic model and thermoacoustic instability results. *Combustion and Flame*, 106:487–510, 1996.

[8] K. K. Kuo. *Principles of Combustion.* John Wiley and Sons, 1986.

[9] J. A. Barnard and J. N. Bradley. *Flame and Combustion.* Chapman and Hall, second edition, 1985.

[10] I. Glassman. *Combustion.* Academic Press, Orlando Florida, USA, 1996.

[11] F. A. Williams. *Combustion Theory.* Benjamin Cummings, Melno Park, California, USA, second edition, 1985.

[12] J. F. Griffiths and J. A. Barnard. *Flame and Combustion.* Blackie Academic and Professional, third edition, 1995.

[13] R. C. Dorf and R. H. Bishop. *Modern Control Systems.* Addison-Wesley Publishing Company, seventh edition, 1995.

[14] J. L. Melsa and D. G. Schultz. *Linear Control Systems.* McGraw-Hill Book Company, 1969.

[15] D.R Hardesty and F. J. Weinberg. Burners producing large excess enthalpies. *Combustion Science and Technology*, 8:201 – 214, 1974.

[16] L. Crocco, J. Grey, and G. B. Matthews. Prelimnary measurements of the combustion time lag in a monopropellant rocket motor. *Fifth Symposium (International) on Combustion*, pages 164–170, 1954.

[17] R. Mohanraj, Y. Neumeier, and B. T. Zinn. Combustor model for simulation of combustion instabilities and their active control. *Journal of Propulsion and Power*, 16(3):485–491, 2000.

[18] F. E. C. Culick. A note on rayleigh's criterion. *Combustion Science and Technology*, 56:159–166, 1987.

[19] A. A. Putnam and W. R. Dennis. A study of burner oscillations of the organ-pipe type. *Transactions of the American Society of Mechanical Engineers*, 75:15–28, January 1953.

[20] A. M. Annaswamy, A. Fleifil, J.P. Hathout, and A.F. Ghoniem. An input output model of thermoacoustic instability and active control design. Report 9705, Dept of Mechanical Engineering, MIT, November 1997.

[21] R.L. Raun, M.W. Beckstead, Finlinson J.C., and K.P. Brooks. A review of rijke burners, and related devices. *Progress in Energy and Combustion Science*, 19:313–364, 1993.

[22] G. A. Richards, M. M. McMillan, R. S. Gemmen, W.A. Rogers, and S. R. Cully. Issues for low emission fuel-flexible power systems. *Progress in Energy and Combustion Science*, 27(2):141–169, 2001.

[23] S. M. Candel. Combustion instabilities coupled by pressure waves and their active control. *Proceedings of the Twenty-Fourth Symposium (International) on Combustion*, pages 1277–1296, 1992.

[24] T. Lieuwen, H. Torres, C. Johnson, and B.T. Zinn. A mechanism of combustion instability in lean premixed gas turbine combustors. *The International Gas Turbine and Aeroengine Congress: Indianapolis, Indiana, ASME*, (99-GT-8), June 1999.

[25] G.J. Bloxsidge and A. P. Dowling. Reheat buzz: an acoustically coupled combustion instability. part 2 theory. *Journal of Fluid Mechanics*, 193:445–473, 1988.

[26] R. Mongia, R. Dibble, and J. Lovett. Measurement of air-fuel ratio fluctuations caused by combustor driven oscillations. *The International Gas Turbine and Aeroengine Congress: Stockholm, Sweden, ASME*, (98-GT-502), June 1998.

[27] A. A. Peracchio and W.M. Proscia. Nonlinear heat-release/acoustic model for thermoacoustic instability in lean premixed combustors. *The International Gas Turbine and Aeroengine Congress: Stockholm, Sweden, ASME,*, (98-GT-502), June 1998.

[28] G. A. Richards and M.C. Janus. Control of flame oscillations with equivalence ratio modulation. *Journal of Propulsion and Power,*, 15(2):232–240, 1999.

[29] T. Lieuwen and B.T. Zinn. The role of equivalence ratio oscillations in driving combustion instabilities in low nox gas turbines. *Twenty seventh Symposium (International) on Combustion*, pages 1809–1816, 1998.

[30] M.R. Murray, C.A. Jacobson, R. Casas, A. I. Khibnik, C. R. Johnson Jr., R. Bitmead, A. A. Peracchio, and W.M. Proscia. System identification for limit cycling systems: A case study for combustion instabilities. *Proceedings of the American Control Conference, 2004-2008, Philadelphia, PA*, June 1998.

[31] G. A. Richards, R. S. Gemmen, and M.J. Yip. A test device for premixed gas turbine combustion oscillations. Technical Note DOE/METC-96/1027, DOE/METC-96/1027,, US DOE Morgantown Energy Technology Center, Morgantown, WV,, March 1996.

[32] J. J. Keller. Thermoacoustic oscillations in combustion chambers of gas turbines. *AIAA Journal*, 33: No 12:2280–2287, 1995.

[33] M. A. Macquisten and A. P. Dowling. Low-frequency combustion oscillations in a model afterburner. *Combustion and Flame*, 94:253–264, 1993.

[34] C. O. Paschereit, E. Gutmark, and W. Weisenstein. Control of thermoacoustic instabilities and emissions in an industrial- type gas-turbine combustor. *Twenty seventh Symposium (International) on Combustion:*, pages 1817–1824, 1998.

[35] O. C. Paschereit, E. Gutmark, and W. Weisentein. Coherent structures in swirling flows and their role in acoustic combustion control. *Physics of Fluids*, 11(9):2667–2678, 1999.

[36] A. P. Dowling. Thermoacoustic instability. *Sixth International Conference on Sound and Vibration, Copenhagen, Denmark,*, July 1999.

[37] H. J. Merk. An analysis of unstable combustion of premixed gases. *Sixth Symposium (International) on Combustion:*, pages 500–512, 1956.

[38] B. D. Mugridge. Combustion driven oscillations. *Journal of Sound and Vibration,*, 70(3):437–452, 1980.

[39] P. L. Blackshear, Jr. Driving standing waves by heat addition. *Fourth Symposium (International) on Combustion:*, pages 553–566, 1953.

[40] V. W. Goldschmidt, R. G. Leonard, J. F. Riley, G. Wolfbrandt, and P. K. Baade. Transfer function of gas flames: Methods of measurement and representative data. *ASHRAE Transactions,*, 84:466:476, 1978.

[41] J. Riley, V. W. Goldschmidt, R. G. Leonard, and P. K. Baade. Noise generation of gas flames due to feedback excited oscillations. *Proceedings of the Third Conference on Natural Gas Research and Technology: Session III paper 5*, March 1974.

[42] J.F. Riley. A transfer function and experimental analysis of feed back excited oscillations in gas flames. Ms thesis, Purdue University,, 1974.

[43] J. D. Antman, R. G. Leonard, V. W. Goldschmidt, and P. K. Baade. Mathematical simulation of feedback excited oscillations in gas combustion systems. *Fluid Mechanics of Combustion,*, pages 7–20, May 1974.

[44] R. Becker and R. Günther. The transfer function of premixed turbulent jet flames. *Thirteenth Symposium (International) on Combustion:*, pages 517–526, 1970.

[45] Y. Matsui. An experimental study on pyro-acoustic amplification of premixed laminar flames. *Combustion and Flame*, 43:199–209, 1981.

[46] A.M. Annaswamy and A. F. Ghoniem. Active control in combustion systems. *IEEE Controls Systems*, pages 49–63, Dec 1995.

[47] M. Fleifil, J. P. Hathout, A. M. Annaswamy, and A. F. Ghoneim. Reduced order modeling of heat release dynamics and active control of time delay instability. *38th Aerospace Sciences Meeting Conference and Exhibit*, (AIAA-2000-0708), January 2000.

[48] G. H. Markstein. *Nonsteady Flame Propagation.* The Macmillan Company Pergamon Press, ,Oxford, England, 1964.

[49] A. H. Nayfeh. *Introduction to Perturbation Techniques*. John Wiley and Sons, 1993.

[50] G. Searby and D. Rochwerger. A parametric acoustic instability in premixed flames. *Journal of Fluid Mechanics*, 231:529–543, 1991.

[51] W. R. Saunders, L. Nord, C. A. Fannin, X. Huang, W. T. Baumann, U. Vandsburger, V. Khanna, L. Haber, B. Eisenhower, and S. Liljenberg. Diagnostics and modeling of acoustic signatures in a tube combustor. *Sixth International Conference on Sound and Vibration, Copenhagen, Denmark*, July 1999.

[52] S. B. Margolis. Bifurcation phenomena in burner-stabilized premixed flames. *Combustion Science and Technology*, 22:143–169, 1980.

[53] A. C. McIntosh. On the cellular instability of flames near porous-plug burners. *Journal of Fluid Mechanics*, 161:43–75, 1985.

[54] G. H. Markstein. Instability phenomena in combustion waves. *Fourth Symposium (International) on Combustion:*, pages 44–59, 1952.

[55] I. R. Hurle, R. B. Price, T. M. Sugden, and A. Thomas. Sound emission from open turbulent premixed flames. *Proceedings of the Royal Society of London, Series A, Mathematical and Physical Sciences*, 303(1475):409–427, March 1968.

[56] S. Hadvig. Combustion instability. system analysis. *Journal of the Institute of Fuel*, pages 550–558, October 1971.

[57] S. Hadvig. Combustion-driven oscillations. *ASME Publication, Paper No.: 73-WA/Fu-5*, November 1973.

[58] M. Ohtsuka, S. Yoshida, S. Image, and N. Kobayashi. Combustion oscillation analysis of premixed flames at elevated pressures. *The International Gas Turbine and Aeroengine Congress, Stockholm, Sweden, ASME*, (98-GT-581), June 1998.

[59] C. O. Paschereit, W. Polifke, B. Schuermans, and O. Mattson. Measurement of transfer matrices and source terms of premixed flames. *The International Gas Turbine and Aeroengine Congress: Indianapolis, USA, ASME*, (99-GT-133), June 1999.

[60] B. B. H. Schuermans, W. Polifke, and C. D. Paschereit. Modeling transfer matrices of premixed flames and comparison with experimental data. *The International Gas Turbine and Aeroengine Congress, Indianapolis, USA, ASME*, (99-GT-132), June 1999.

[61] D. Bohn, G. Deutsch, and U. Kruger. Numerical prediction of the dynamic behavior of turbulent diffusion flames. *Journal of Engineering for Gas Turbine and Power*, 120:713–720, October 1998.

[62] D. Bohn, Y. Li, and G. Matouschek. Numerical prediction of the dynamic behior of premixed flames using systematically reduced multistep reaction mechanism. *The International Gas Turbine and Aeroengine Congress, Florida, USA, ASME*, (97-GT-265), June 1997.

[63] J. O. Keller and C. K. Westbrook. Response of a pulse combustor for changes in fuel composition. *Twenty-first Symposium (International) on Combustion*, pages 547–555, 1986.

[64] J. O. Keller, T. T. Bramlette, J. E. Dec, and C. K. Westbrook. Pulse combustion: Importance of characteristic times. *Combustion And Flame*, 75:33–44, 1989.

[65] U. Vandsburger, K. McManus, and C. Bowman. Effects of fuel spray vaporization on the stability characteristics of a dump combustor. *Twenty-Fifth Joint Propulsion Conference, Monterey, CA,USA*, (AIAA-89-2436), July 1989.

[66] J. Mehta, W. Dodds, and D. Bohr. Fuel effects on gas turbine combustor dynamics. *Twenty-Sixth Joint Propulsion Conference, Orlando, Florida,USA*, (AIAA-90-1957), July 1990.

[67] M. C. Janus, G. A. Richards, and M. J. Yip. Effects of ambient conditions and fuel composition on combustion stability. *The International Gas Turbine and Aeroengine Congress, Florida, USA, ASME*, 1997.

[68] R. M. Flores, M. M. Miyasato, V. G. McDonell, and G. S. Samuelsen. Response of a model gas turbine combustor to variation in gaseous fuel composition. *The International Gas Turbine and Aeroengine Congress, Munich, Germany, ASME*, (2000-GT-0141), May 2000.

[69] S. E. Habik. The effect of hydrogen and ethane addition on polluting emissions and burning velocity in propane air flame. *Journal of Engineering and Applied Science*, 45(3):375–391, June 1998.

[70] L. C. Haber. An investigation into the origin, measurement and application of chemiluminescent light emissions from premixed flames. Master's thesis, Virginia Polytechnic Institute and State University, march 2001.

[71] Jarrel-Ash. *Model 82 - 000 Series 0.5 M Ebert Scanning Spectrophotometer*. Waltham MA 02154, 1971.

[72] M. P. Waser and M. J. Crocker. Introduction to the two-microphone cross-spectral method of determining sound intensity. *Noise Control Engineering Journal*, April 1984.

[73] National Instruments. *LabVIEW User Manual Part No 320999 A - 01*, 1996.

[74] Hasings Instruments. *Hastings Model HFM Mass Flow-Meters*. Teledyne Brown Engineering - Hastings Instruments, P.O. Box 1436, Hampton, VA 23661, USA, 1994.

[75] R. J. Lee, J.F. Grcar, M.D. Smooke, and J. A. Miller. A fortran program for modeling steady laminar one-dimensional premixed flames. *SAND85-8240, Combustion Chemistry Division Sandia Laboratories*, Dec 1986.

[76] L Nord. A thermoacoustic characterization of a rijke-type tube combustor. Master's thesis, Virginia Polytechnic and State University, Blacksburg, VA. USA, Feburary 2001.

[77] G. P. Smith, D. M. Golden, M. Frenklach, N. W. Moriarty, B. Eiteneer, M. Goldenberg, C. T. Bowman, R. K. Hanson, S. Song, W. C. Jr. Gardiner, V. V. Lissianski, and Z. Qin. $http://www.me.berkeley.edu/gri_mech/$.

[78] P. Dagaut, J. Luche, and M. Cathonnet. Experimental and kinetic modeling of the reduction of no by propene at 1 atm. *Combustion and Flame*, 121:651–661, 2000.

[79] A. A. Labs, Isreal. *AN-1003 Hotwire and Film Anemometry System.*

[80] A. K. Gupta, D. G. Lilley, and N. Syred. *Swirl Flows.* Abacus Press, June 1985.

[81] M. M. Ribeiro and J. H. Whitelaw. Coaxial jets with and without swirl. *Journal of Fluid Mechanics*, 96(4):769–795, 1980.

[82] T. C. Claypole and N. Syred. The effect of swirl burner aerodynamics on NO_x formation. *Eighteenth Symposium International on Combustion*, pages 81–89, 1981.

[83] D. Feikema, R. H. Chen, and J.F. Driscoll. Enhansement of flame blowout limits using swirl. *Combustion and Flame*, 80:183–195, 1990.

[84] T. Lieuwen, Y. Neumier, and B. T. Zinn. The role of unmixedness and chemical kinetics in driving combustion instabilities in lean premixed combustors. *Combustion Science and Technology*, 135:193–211, 1998.

[85] W. Shih, J. G. Lee, and D. A. Santavicca. Stability and emissions characteristics of a lean premixed gas turbine combustor. *Twenty sixth Symposium (International) on Combustion*, pages 2771–2778, 1996.

[86] B. M. Kumar and R. I. Sujith. Exact solution for one-dimensional acoustic fields in ducts with polynomial temperature profiles. *Journal of Vibrations and Acoustics*, 120:965–969, 1998.

[87] T. Lieuwen and B. T. Zinn. Application of boundary element methods in modeling multidimensional flame-acoustic interactions. *20th World Conference on the Boundary Element Method*, August 1998.

[88] N. T. Davis and G. S. Samuelsen. Optimization of gasturbine combustor performance throughout the duty cycle. *Twenty sixth Symposium (International) on Combustion*, pages 2819–2825, 1996.

[89] Burr-Brown. Burr-brown technical information. Technical report, http://www.burrbrown.com.

[90] J. W. Barnes. *Statistical Analysis for Engineers and Scientists :- A Computer based Approach*. Mc-Graw Hill, 1994.

[91] R. Siegel and J. R. Howell. *Thermal Radiation Heat Transfer*. Hemisphere Publishing Corporation, Washington, D.C, USA., third edition, 1990.

[92] A. H. Lefebvre. *Gas Turbine Combustion*. Hemisphere Publishing Corporation, 1983.

[93] M. A. Vaudrey. *Adaptive Control Methods for Self-Excited Systems*. PhD thesis, Virginia Polytechnic Institute and State University, Blacksburg, VA., USA, August 2001.

Vita

Vivek Khanna was born in Jamshedpur, India in 1967. He graduated from St. Vincent's High School, Pune, India in 1984. He pursued his Bachelor's degree in Mechanical Engineering at University of Poona, which he completed in 1988. For the next two years, he worked at Sandvik Asia Ltd. Pune, India as a production Engineer gaining experience in manufacture and design of special cutting tools. In fall of 1990, he joined the graduate program in Mechanical Engineering at University of Texas at Austin, Austin Texas. There he worked under Dr. Janet Ellzey and Dr. John R. Howell on a research project related to radiant burners and completed his Masters of Science in Mechanical Engineering in August 1992. For the next six years, he was Executive Director of Thermal Technologies (India) Pvt. Ltd. that designed and manufactured heat exchangers and pressure vessels. He was responsible for the startup of this company and all its operations. In fall of 1998, he joined the Virginia Active Control and Combustion Group at Virginia Tech to pursue his PhD under the guidance of Dr. Uri Vandsburger. While pursuing his degree, he was an instructor for the undergraduate heat transfer class during the summer of 1999. Upon completion of his PhD, he will begin working at Solar Turbines, A Caterpillar Company at San Diego, CA.